Heat flux distribution on the XCPC absorber of an external compound parabolic solar collector

ST Simon, MTF Owen and JP Meyer*

Department of Mechanical and Mechatronic Engineering, Stellenbosch University, Stellenbosch, 7600, South Africa

Email: jpm2@sun.ac.za

Abstract: This study investigates the heat flux distribution on the absorber (upper and lower) tube and fin of an external compound parabolic collector (XCPC). Two-dimensional radiation simulations were conducted in ANSYS Fluent 2023 R2 using the Discrete Ordinates (DO) method in Finite Volume (FV) to quantify the incident radiation on the pentagon-shaped fin and absorber tube. This method simultaneously solves each iteration's radiative transport equation (RTE). The 2D DO method is known for its accuracy in identifying scattering effects but has limitations, such as false scattering and ray effects which can reduce the accuracy of the results. However, measures have been implemented in literature to address these challenges. The number of cells in the 2D DO simulation ranged from 13 071 to 418 276 to assess the impact of false scattering in the mesh sensitivity analysis for the fin and tube sections. A cell count of 209 138 cells was selected to balance computational cost and time while reducing uncertainty. The angular discretization study investigated different division levels on the 209 138 cells, ranging from coarse (2×2) to fine (3×200), while keeping a constant 3×3 pixelation across all simulations. The results showed that from the 3×30 divisions onward, the simulation curves for the tube sections and fin began to overlap. The 3×100 discretization was chosen as it provided reliable results without requiring excessive computational time.

Keywords: external compound parabolic concentrator; ANSYS Fluent; radiation transport equation; ray effects; false scattering

1. Introduction

The external compound parabolic collector (XCPC) is a non-imaging solar collector that uses line-focus concentration for low to medium temperature applications (60℃ to 300℃) with a concentration ratio of 1.4. The XCPC collector comprises a compound parabolic reflector and an evacuated receiver tube with a direct flow U-shaped absorber tube attached to a pentagonal fin as shown in **Fig. 1**. The literature extensively examines distinct reflector designs and optical components of CPCs thus contributing to the evolving landscape of CPC technology [1-3].

Korres et al [2] developed a numerical model using SolidWorks to analyse the heat transfer performance of a CPC. The study investigated the temperature and pressure distribution and identified secondary flow in the U-bend of the U-type circular-shaped absorber but did not discuss the incident radiation on the absorber in detail.

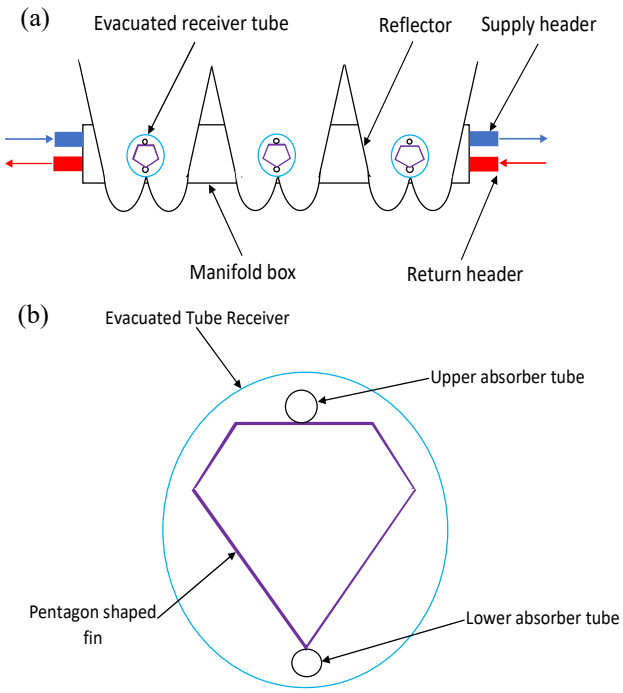

Fig. 1: (a) The front view of the XCPC shows the fluid flow distribution within the collector, indicated by blue and red arrows. (b) The detailed view of the evacuated receiver tube comprises an upper and lower absorber tube attached to the fin. (Not drawn to scale).

Widyolar et al [1, 3] developed a theoretical model of an XCPC prototype to evaluate its performance. While their study considers incident radiation and radiation losses in the performance model, it does not provide any information on the circumferential distribution of the absorber tube and fin. Moghimi et al [4-6] used the 2D discrete ordinate (DO) method to assess the circumferential non-uniform heat flux distribution in a Linear Fresnel Collector. The authors identified two key challenges with the DO method: false scattering and the ray effect. Various approaches were explored to improve the accuracy of the numerical results. Despite these contributions, no studies focus on the heat flux distribution in an XCPC with its unique absorber tube and fin geometry. Therefore, this study aims to determine the circumferential non-uniform heat flux

distribution on the absorber (fin and tube) of an external compound parabolic concentrator. This work forms part of a larger study that examines the local heat transfer and pressure drop characteristics inside the U-type absorber tube, subject to non-uniform heat flux under laminar flow conditions.

2. Methodology

The discrete ordinates (DO) radiation method for finite volume (FV) [4-6] was selected in ANSYS Fluent 2023 R2 to quantify the circumferential incident radiation distribution on the tube sections and fin. This method solves the radiative transport equation (RTE) and the energy equation. There are several advantages to using the DO radiation model. It is easy to implement using the finite volume (FV) framework, efficiently handles various boundary conditions and offers flexibility in adjusting 2D geometries. However, the DO method has two primary challenges documented in the literature [4-6]: the ray effect (also called ray concentration errors) and false scattering [7]. The ray effect occurs when the radiation beam propagation is discretized into a limited number of solid angle directions leading to inaccuracies. This can be prevented by using a higher number of ordinate directions in solving the RTE (ANSYS Fluent uses a fixed ordinates approach) or refining the angular discretization divisions. False scattering happens when numerical diffusion leads to radiation being incorrectly scattered across different directions. This can be prevented by increasing the cell count, using a higher order spatial discretization scheme or refining the spatial mesh. Several analyses were carried out using the 2D DO method for this study to address these challenges. This involved comparing first and second-order upwind schemes for spatial discretization, performing a mesh sensitivity analysis by doubling cell counts (up to 418 276 cells) and assessing the impact of varying control angles ($N_\theta \times N_\Phi$) on angular discretization. The method for solving the DO equation involved a SIMPLE pressure-velocity coupling scheme and second-order spatial discretization for both the momentum and energy equations. Simulations were run for 1 000 iterations to ensure that residuals had converged and stabilized. These radiation fluxes were plotted around the circumference of the tube section and fin.

2.1 *Gray and non-grey radiation*

Gray radiation assumes that a material's radiative properties such as the spectral emissivity and absorptivity are constant across all wavelengths. In contrast, non-gray radiation accounts for wavelength-dependent variations in these properties, providing a more accurate but complex model [4, 5]. Gray radiation is chosen in the DO model because variations in radiative properties over the relevant wavelengths are minimal and do not significantly impact the heat flux distribution in the XCPC collector

2.2 *Angular discretization and pixelation*

Solving the radiative transport equation (RTE) in three dimensions requires substantial computational resources. As a result, the 2D simulation approach becomes a more practical alternative while maintaining accuracy. The RTE shown in **Eq. 1** is solved in the global Cartesian coordinate system where the angular space is discretized into subdivisions defined as $N_\theta \times N_\Phi$. These represent the polar (θ) and azimuthal (Φ) angular divisions of the solid angles measured relative to the global Cartesian system [4].

Each solid angle subdivision is divided into smaller sections, which are known as pixelation, as illustrated in **Fig. 2**. The pixelation is denoted by $Pixel_\theta \times Pixel_\Phi$ where each subdivision consists of θ and Φ divisions. The default pixelation setting of 1×1 is generally sufficient for Gray-diffuse radiation. However, considering the symmetry and semi-transparent boundary conditions in the DO model, a finer pixelation of 3×3 was recommended in the ANSYS user guide [8]. This setting was applied consistently across all simulations.

The RTE is mathematically written as:

$$\nabla \cdot (I(\vec{r} \cdot \vec{s})\vec{s}) + (a + \sigma_s)I(\vec{r} \cdot \vec{s}) = an^2 \frac{\sigma T^4}{4\pi} + \frac{\sigma}{4\pi}\int_0^{4\pi} I(\vec{r} \cdot \vec{s}')\Phi(\vec{s} \cdot \vec{s}')d\,\Omega' \quad (1)$$

The first term on the left-hand side of the equation represents the rate of change of irradiation, while the second term represents absorption. On the right-hand side, the first term represents emission and the second term deals with scattering. The a, σ_s are the absorption and scattering coefficients, n is the refractive index, I is the radiation intensity, Φ is the scattering phase function, Ω' is the solid angle, T represents the local temperature and σ is the Stefan-Boltzmann constant (5.678×10^8 W/m^{2}k). The vector $\vec{r}$ is the cartesian coordinate in space in the x and y direction and $\vec{s}$ is a unit vector in the direction of the beam shown in the global cartesian system in **Fig. 2**. The scattering coefficient, the scattering phase function and the refractive index are assumed independent of the wavelength [4-6].

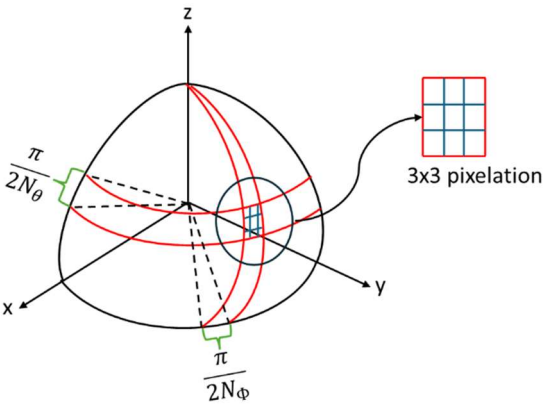

Fig. 2: The angular discretization of the 2D DO method (adapted from [4])

The radiative term ($q'''_{radiation}$) was included to account for the net loss of radiative energy in **Eq. 2**. ANSYS Fluent solved this term and the RTE (**Eq. 1**),

simultaneously to model radiation emission and absorption.

The energy equation for solar radiation was solved in 2D and is expressed as [4]:

$$u\frac{\partial(\rho C_p T)}{\partial x} + v\frac{\partial(\rho C_p T)}{\partial y} = \frac{\partial}{\partial x}\left(k\frac{\partial T}{\partial x}\right) + \frac{\partial}{\partial y}\left(k\frac{\partial T}{\partial y}\right) + q'''_{radiation} \quad (2)$$

Where k is the thermal conductivity, ρ is the density, C_p is the specific heat capacity, u and v are the velocity components in the x and y directions.

.

2.3 *Spatial discretization*

The accuracy of the numerical results and potential false scattering errors [4-6] are affected by the order of discrete ordinates used in the spatial discretization methods. To minimize false scattering error, the effect of smearing was investigated and the corresponding plots are shown in **Fig. 3**. The angular discretization was set at $N_\theta \times N_\Phi = 3 \times 40$ and a cell count of 209 138 cells was used.

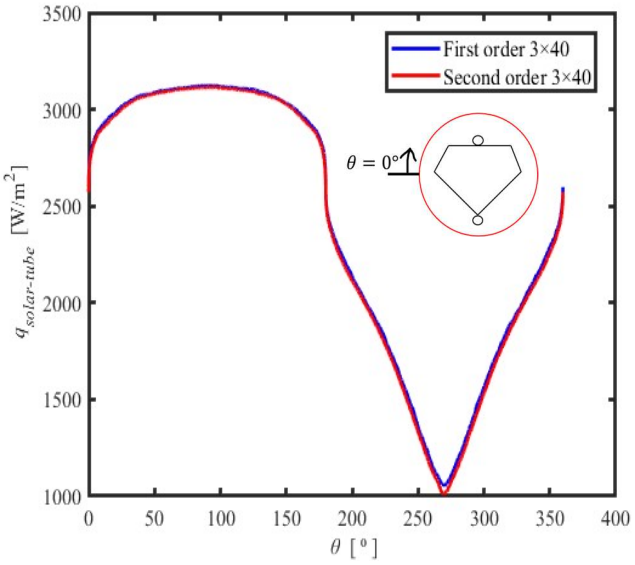

Fig. 3: The effect on the incident radiation distribution on the evacuated receiver tube using the first and second order discrete ordinates.

Fig. 3 shows the effect of spatial discretization order on incident radiation along the circumference of the evacuated receiver tube. At θ = 90°, the incident radiation was 3 120 W/m^2 for first order and 3 111 W/m^2 for second order with a 0.3% difference. At θ = 270°, the incident radiation was 1 051 W/m^2 for first order and 1 010 W/m^2 for second order with a 4% difference. Given the small difference between the first and second-order discretization, the second-order upwind scheme was chosen for its more refined solution and reduced smearing compared to the first order discretization.

2.4 Verification

A mesh sensitivity analysis was conducted to evaluate the impact of cell count on numerical results using a fixed 3×100 angular discretization and 3×3 pixelation as mentioned in the previous section. The cell counts in the 2D DO simulation were doubled ranging from 13 071 to 418 276 cells. The mesh resolution was adjusted from the coarsest (13 071 cells) to the finest (418 276 cells). The incident radiation at θ = 185° was selected for analysis on both the upper and lower tube sections, as this region was unshaded and fully exposed to radiation.

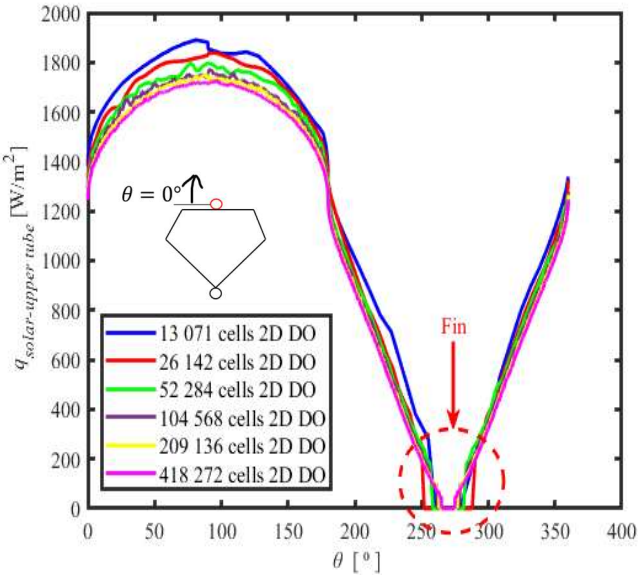

Fig. 4: The incident radiation on the circumference of the upper absorber tube in contact with the fin.

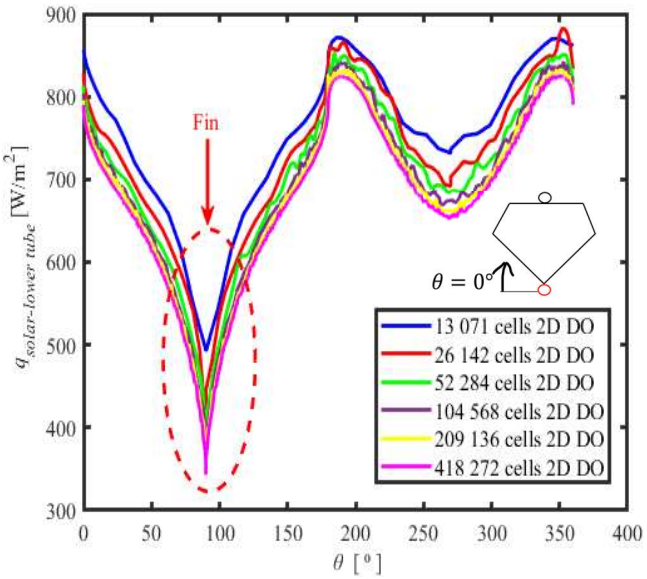

Fig. 5: The incident radiation on the circumference of the lower absorber tube in contact with the fin.

At θ = 185° for the upper tube in **Fig. 4**, the incident radiation was 1 202 W/m^2 with 13 071 cells and 1 087 W/m^2 with 418 276 cells showing a 10% difference. With 104 569 and 209 138 cells, the difference relative to the 418 276 cells dropped to 2.3% and 1.6%, respectively. For the lower tube at θ = 185° in **Fig. 5**, the incident radiation was 870 W/m^2 with 13 071 cells and 821 W/m^2 with 418 276 cells showing a 5.8% difference. With 104 569 and 209 138 cells, the

difference relative to the 418 276 cells decreased to 1.2% and 0.5%, respectively. Tube sections in contact with the fin received no direct radiation on parts of the upper tube, while the lower tube had partial exposure due to point contact with the fin.

Refining the mesh and increasing the cell count further helps reduce false scattering errors. However, as the number of cells in the mesh doubles, the computational time also increases accordingly. The solution for the incident radiation on the upper and lower tube becomes independent with uncertainty remaining below 3% for meshes of 100 000 cells and above. Therefore, 209 138 cells were selected as the optimal mesh size to balance computational cost, accuracy and time. Mesh refinement helps reduce false scattering which is further minimized using second-order discretization.

3. Validation of the DO model.

The discrete ordinates (DO) model was validated by comparing its geometric efficiency with that of Widyolar et al [1, 9]. The authors also used a particular reflector design and classified the upper and lower absorber tubes and the fin as a single "absorber". For this DO validation, normal incidence radiation of 1 000 W/m^2 was applied and the geometric efficiency was calculated as the ratio of absorbed radiation on the absorber to the total incident radiation on the aperture (reflector). The resulting geometric efficiency in this study was 90.4%, while Widyolar was 94% (obtained using LightTools for ray tracing analysis). This close alignment suggests that the DO model effectively predicts radiation absorption in the collector and can be reliably used to quantify solar fluxes around the circumference of the tube sections and fin.

4. Setup, boundary conditions and meshing of the 2D DO model

The 2D geometry illustrated in **Fig. 6** participates in the DO ray tracing radiation. It consists of a pentagon-shaped fin, an upper and lower absorber tube, a reflector profile and an evacuated receiver tube. There are two symmetry walls at the ends of the parabolic reflector, extending outward on opposite sides and connecting the radiation source at the top. The fin and absorber tube are solid copper, while the reflector wall is aluminum with specific thermal properties of the materials summarized in **Table 1**. There is a gap between the bottom of the absorber tube and the tip of the reflector. In the modelling shown in **Fig. 6**, this gap has been minimized to 3 mm, as done by Widyolar et al [1, 9]. This adjustment allows for a 0.8 mm space between the lower absorber and inner glass tubes.

The radiative properties consist of absorptance, emittance, reflectance and transmittance. These properties are specified at each domain (solid) in the cell zone conditions [4]. By the first law of thermodynamics, the sum of these properties must be exactly one. The radiative surface equation can be written as:

$$\alpha + \rho + \tau = 1 \quad (3)$$

Where α is the absorptivity, ρ is the reflectivity and τ is the transmissivity. For opaque walls, transmissivity is zero ($\tau = 0$). Therefore **Eq. 4** combined into **Eq. 3** can be written in terms of reflectivity:

$$\rho = 1 - \varepsilon \quad (4)$$

Where ε is the emissivity.

Table 1: The material properties used in the DO modelling

Material	Domain	Properties
Reflector wall	Solid	ρ = 2 719 kg/m^3 C_p = 871 J/kg K k = 202.4 W/m K
Absorber tube(s) and Fin	Solid	ρ = 8 978 kg/m^3 C_p = 381 J/kg K k = 387.6 W/m K
Evacuated glass tube	Solid	ρ = 2 124.9 kg/m^3 C_p = 779.74 J/kg K k = 1.15 W/m K
Air	Fluid	ρ = 1.23 kg/m^3 C_p = 1 006.43 J/kg K k = 0.024 W/m K

The absorber tube in the geometry has an inner diameter of 6.5 mm, an outer diameter of 8 mm and a thickness of 0.75 mm. The fin, shaped like a pentagon, has a perimeter of 272 mm. The absorber tube, fin and reflector wall are modelled as opaque surfaces with a specified temperature of 1 K, as done by Moghimi et al [4-6] to model walls as cold in their respective solid domain. This approach prevents thermal re-radiation from the surface and isolates the incident solar heat flux. The fin and absorber tube are coated with a high absorptance coating (Sunselect) of 0.95 to absorb solar radiation on the tube and an emissivity of 0.05 [1]. The fin and absorber tube have a refractive index of 0.22 and an absorption coefficient of 1.39 m^{-1} [10]. The Mylar reflector has a reflectivity of 0.89 and an emissivity of 0.11 [1, 3]. The reflector has a refractive index of 1.4 and an absorption coefficient of 2.71 m^{-1} [10]. The radiation source is modeled using a semi-transparent boundary condition for thermal radiation. The radiation source has beam angles of θ = 0.53° and Φ = 0.53° with its beam direction along the -Y axes (X = 0, Z = 0). At normal incidence, it has a direct irradiation value of 1 000 W/m² parallel to the beam direction. The external emissivity was set to 1 and the external radiation temperature was 1 K.

The evacuated receiver tube is modelled as a semi-transparent wall boundary condition, made of solid borosilicate glass with a refractive index of 1.5 and an absorption coefficient of 18 m^{-1} [4]. This absorption coefficient of glass was calculated relative to its absorptivity as:

$$\alpha = 1 - \tau = 1 - e^{-as} \quad (5)$$

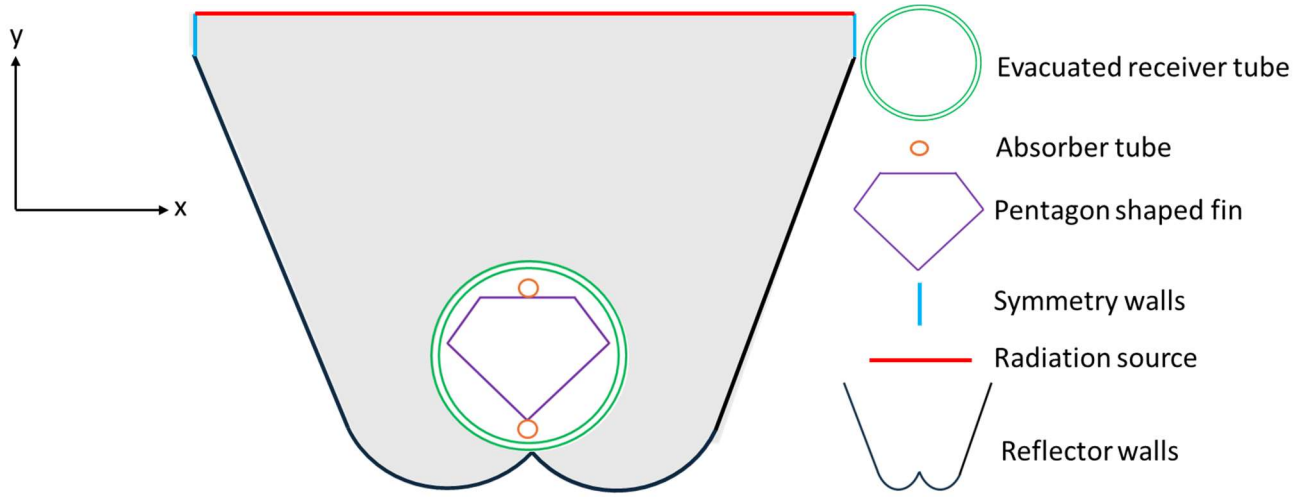

Fig. 6: The 2D D0 model outlines the structure of the collector and its component features used in the radiation modelling. (Not drawn to scale)

Where s is the thickness of the evacuated receiver tube.

The interior of the glass tube where the fin and tube are located is evacuated. The space between the reflector and the evacuated receiver tube is simulated as a "fluid" with the thermal properties of air. The air has a refractive index of 1 and is assumed to be transparent to radiation with an absorption coefficient of 0 [5]. The gravitational acceleration is 9.81 m/s^2 in the opposite y direction.

The diffuse fraction parameter in ANSYS Fluent is set to 1 (f_d = 1), meaning that the surface reflects radiation in a purely diffuse manner. This assumption suggests that the surface emits the same amount of radiation in all directions, unlike a specular surface that reflects light in a specific direction. The mesh quality metrics such as the orthogonality quality, aspect ratio, element quality and skewness meet the standards set by the ANSYS user guide [8]. Therefore, the numerical results obtained are reliable for comparisons. In the mesh sensitivity study, the divisions in ANSYS Fluent meshing were modified to effectively control the cell count, which was doubled at each division.

4. Results on the angular independence discretization study.

The influence of the ray effect is evident in the numerical results for the upper and lower tube and the fin as shown in **Figs. 7, 8** and **9**. Increasing the magnitude of the theta and phi divisions (control angles) improves the accuracy of the results, but the refined results overlap after increasing them beyond a certain increment which would result in additional computational time and cost. Therefore, the angular discretization increments of N_θ being 2 and 3 were only considered in this paper. This assumption is based on two-dimensional planar coordinates for the second order DO. The angular discretization varied from the coarsest (2×2) to the finest (3×200). The different increments of the angular discretization were evaluated at θ = 45° for the upper and lower tube and Δs = 0.1 m for the fin using 209 138 cells from the mesh sensitivity analyses.

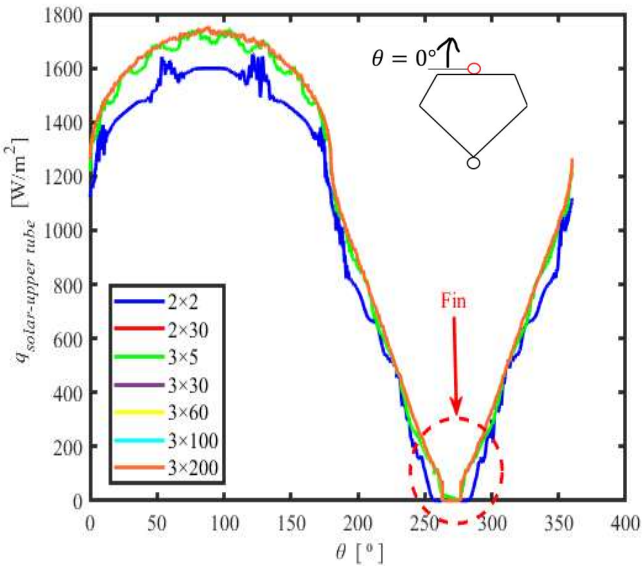

Fig. 7: Incident radiation on the circumference of the upper absorber tube at different angular discretization.

At θ = 45° for the upper tube in **Fig. 7**, the incident radiation was 1 477 W/m^2 for 2×2 angular discretization and 1 658 W/m^2 for 3×200, showing a 12% difference. For simulations with 3×30 and 3×100 discretization, the difference relative to the 3×200 decreased to 0.5% and 0.4%, respectively. The results show slight ray effects due to the angular discretization. At θ = 45° for the lower tube in **Fig. 8**, the incident radiation was 572 W/m^2 for 2×2 angular discretization and 638 W/m^2 for 3×200 showing an 11% difference. For simulations with 3×30 and 3×100 discretization, the difference relative to the 3×200 decreased to 0.4% and 0.2%, respectively. There are fluctuations in the incident radiation at different angular discretization from

$200° < \theta < 330°$ on the lower absorber tube. The coarsest angular discretization of 2×2 shows discontinuities and ray effects. As the angular discretization is refined from 2 to 3 increments, the solution becomes more accurate and converges when the azimuth angle exceeds 30° ($\Phi > 30°$).

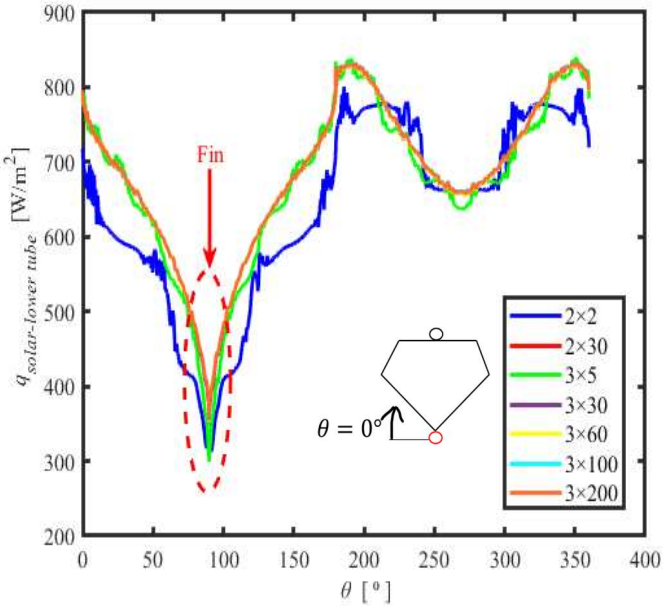

Fig. 8: Incident radiation on the circumference of the lower absorber tube at different angular discretization.

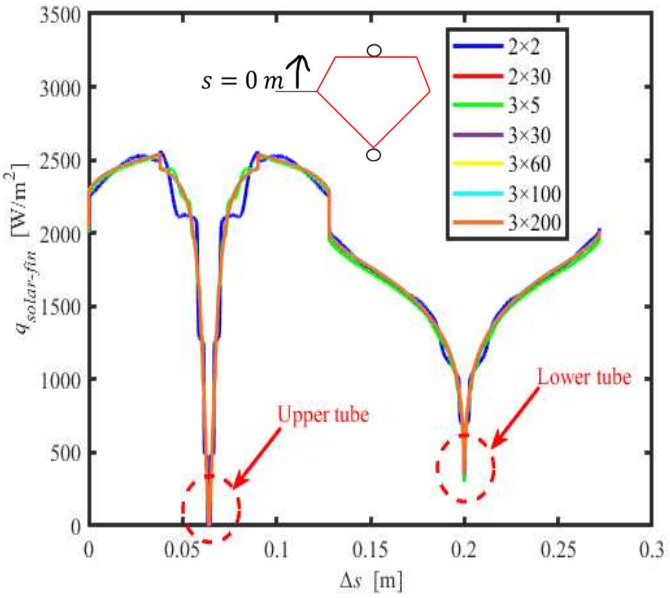

Fig. 9: Incident radiation on the circumference of the fin at different angular discretization.

At $\Delta s = 0.1$ m for the fin in **Fig. 9**, the incident radiation was 2 527 W/m^2 for 2×2 angular discretization and 2 502 W/m^2 for 3×200 showing a 1% difference. For simulations with 3×30 and 3×100 discretization, the difference relative to the 3×200 decreased to 0.2% and 0.1%, respectively.

Increasing the angular discretization helps reduce the ray effect error. A polar (or theta) increment of 2 contributed to the ray effect with the 2×2 grid (shown in blue) producing results that neither matched the other numerical results nor generated a similar profile for the fin and tube sections. As the theta divisions increased to 3 and the phi divisions ranged from 30 to 200, no noticeable differences were observed in the incident radiation. The $N_\theta \times N_\Phi$ of 3×200 was found to be the most accurate and yet the most time-consuming. Therefore, the 3×100 discretization was selected for further analysis in the DO modelling as it required less computational time than 3×200 and the uncertainty for both configurations on the upper and lower tubes and fin was minimal.

5. Conclusion

This study aimed to develop flux distributions for the fin and the upper and lower absorber tubes in an XCPC collector. After validating the model through sensitivity analyses, the flux distribution showed high and low concentration areas consistent with the concentration ratio. These findings will be used in future research to evaluate the U-type absorber tube's heat transfer characteristics and friction factors.

Acknowledgment

The funding received from STERG, Stellenbosch University, is acknowledged and greatly appreciated by the authors.

Reference(s)

1. B. Widyolar, L. Jiang, J. Ferry, R. Winstown, Non-tracking East-West XCPC solar thermal collector for 200 celsius applications. Applied Energy, 2018. **216**: p. 521-533.
2. D. Korres, C. Tzivanidis, A new mini-CPC with a U-type evacuated tube under thermal and optical investigation. Renewable Energy, 2018. **128**: p. 529-540.
3. B. Widyolar, L. Jiang, Y. Bhusal, J. Brinkley, R. Winston, Solar thermal process heating with the external compound parabolic concentrator (XCPC) 45 m^2 experimental array performance, annual generation (kWh/m^2-year), and economics. Solar Energy, 2021. **230**: p. 131-150.
4. K. Craig, M. Moghimi, A. Rungasamy, J. Marsberg, J.P. Meyer, Finite-volume ray tracing using Computational Fluid Dynamics in linear focus CSP applications. Applied Energy, 2016. **183**: p. 241-256.
5. Moghimi, M., K. Craig, and J.P. Meyer, A novel computational approach to combine the optical and thermal modelling of Linear Fresnel Collectors using the finite volume method. Solar Energy, 2015. **116**: p. 407-427.
6. K. Craig, M. Moghimi, J.P. Meyer, Simulation-based optimisation of a linear Fresnel collector mirror field and receiver for optical, thermal and economic performance. Solar Energy, 2017. **153**: p. 655-678.

7. H.S. Li, Reduction of false scattering in arbitrarily specified discrete directions of the discrete ordinates method. Journal of Quantitative Spectroscopy and Radiative Transfer, 2004. **86**(2): p. 215-222.
8. Manual, U, ANSYS FLUENT 12.0. Theory Guide, 2009. **67**.
9. B. Widyolar, L. Jiang, A. Hassanzadeh, R.Winstown, Compound parabolic concentrator for pentagon shape absorber. in Proceedings of the ISES Solar World Congress. 2017.
10. I. Suleiman, Determination of linear absorption coefficient for different materials. Int. J. Modern Res. Eng. Technol., 2018. **3**: p. 28-38.